

## ARTICLE

## Compositional Engineering of Metal-Xanthate Precursors toward $(\text{Bi}_{1-x}\text{Sb}_x)_2\text{S}_3$ ( $0 \leq x \leq 0.05$ ) Films with Enhanced Room-Temperature Thermoelectric Performance

Received 00th January 20xx,  
Accepted 00th January 20xx

DOI: 10.1039/x0xx00000x

Zhenyu Hu,<sup>abc</sup> Longhui Deng,<sup>bc</sup> Tingjun Wu,<sup>c</sup> Jing Wang,<sup>d</sup> Feiyan Wu,<sup>d</sup> Lie Chen,<sup>d</sup> Qikai Li,<sup>e</sup> Weishu Liu,<sup>e</sup> Shui-Yang Lien,<sup>f</sup> Peng Gao,<sup>bc\*</sup>

The preparation of high-performance thermoelectric thin films can be challenging. Herein, we report the preparation, characterization, and thermoelectric performance of morphology-controlled bismuth sulfide ( $\text{Bi}_2\text{S}_3$ ) thin films using a single-source precursor called bismuth (III) ethylxanthate, with which the room-temperature thermoelectric thin-film can be prepared quickly and cost-effectively. We acquired the intrinsic  $\text{Bi}_2\text{S}_3$  thin films with electrical conductivity of  $14.23 \text{ S m}^{-1}$  and a Seebeck coefficient of  $-388.33 \mu\text{V K}^{-1}$  at room temperature, comparable to the bulk  $\text{Bi}_2\text{S}_3$ . Furthermore, a higher Seebeck coefficient can be achieved by adopting a composition engineering method to achieve antimony (Sb)-doping solid solution, in which phonon scattering and dislocation density can be manipulated. By tuning the mole fraction of Sb in the films, we further improved the Seebeck coefficient to  $-516.35 \mu\text{V K}^{-1}$  and the power factor to  $170.10 \mu\text{W m}^{-1} \text{ K}^{-2}$  with a solid solution of  $(\text{Bi}_{0.97}\text{Sb}_{0.03})_2\text{S}_3$ . Thus, the chalcogenide composition engineering protocol could be a universal methodology to make target semiconductors for thin-film thermoelectric applications, which may broaden the application of thermoelectric films in the field of microelectronic devices.

### Introduction

The past decade has witnessed endeavors to search for alternative energy sources and further circumvent the energy crisis and environmental deterioration.<sup>1–3</sup> For the sake of the future of human beings, it is urgent to transform the paradigm of energy consumption by seeking alternative energy harvesting approaches. With the efforts of researchers, environmentally friendly energy sources like solar,<sup>3,4</sup> hydropower,<sup>5,6</sup> nuclear power,<sup>7,8</sup> and geothermal energy,<sup>9,10</sup> etc., emerged over the past several decades. Since the discovery of the thermoelectric effect by Thomas Seebeck,<sup>11</sup> thermoelectric generators (TEGs) have attracted significant interest because of their unique ability to convert waste heat to electrical energy directly.<sup>12–14</sup> The performance of a TEG is related to the efficiency of the thermoelectric (T.E.) materials, which in turn is proportional to a dimensionless figure-of-merit ( $ZT$ ).  $ZT$  is defined as  $ZT = (S^2\sigma T)/\kappa$ , where  $S$  is the Seebeck coefficient,  $\sigma$  is the electrical conductivity,  $\kappa$

is the thermal conductivity, and  $T$  is the absolute temperature.<sup>15,16</sup> When the thermoelectric materials are fabricated in the form of thin films, the power factor ( $P.F.$ ), as defined by  $P.F. = S^2\sigma$ , is normally used as the indicator for evaluating thermoelectric performance.<sup>17–19</sup>

Theoretically, thermoelectric films (TEFs) are expected to have lower thermal conductivity than that of the bulk materials due to stronger phonon scattering at both surface and film/substrate interface.<sup>20–22</sup> This advantage endows the TEFs great potential in developing high-performance and inexpensive thermochemical chips and cooling systems for microelectronic components.<sup>23</sup> So far, the best material for room-temperature thermoelectrical applications is bismuth telluride ( $\text{Bi}_2\text{Te}_3$ ) and its alloys in both bulk and thin-film forms.<sup>24</sup> However, the toxic and rare tellurium (Te) element may limit the prevailing application of the compounds, so that scientists must seek cheaper and nontoxic alternatives.

Sulfur (S), on the other hand, is abundant in the Earth's crust, inexpensive, and has low toxicity. Therefore, substituting bismuth sulfide ( $\text{Bi}_2\text{S}_3$ ) for bismuth telluride ( $\text{Bi}_2\text{Te}_3$ ) is feasible for room-temperature T.E. applications.  $\text{Bi}_2\text{S}_3$ , with a direct bandgap of 1.3 eV,<sup>25–27</sup> belongs to the family of compounds  $\text{M}_2\text{X}_3$  (where  $\text{M} = \text{Bi}, \text{Sb}$ , and  $\text{X} = \text{S}, \text{Se}, \text{Te}$ ), which are considered to be promising candidates for thermoelectric applications. Various methods toward  $\text{Bi}_2\text{S}_3$  thin films have been reported, including chemical bath deposition (CBD),<sup>28,29</sup> chemical vapor deposition (CVD),<sup>30,31</sup> spray pyrolysis (S.P.),<sup>32,33</sup> dip-coating technology,<sup>34</sup> and successive ionic layer adsorption and reaction (SILAR).<sup>35,36</sup> However, films based on these methods showed inferior electrical transport properties, discouraging further research on their thermoelectric properties. For example, Recatala-Gomez et al. prepared  $\text{Bi}_2\text{S}_3$  thin film by electron beam lithography with an electrical conductivity of  $6 \text{ S cm}^{-1}$ , which

<sup>a</sup> College of Chemistry, Fuzhou University, Fuzhou, Fujian, 350108, China

<sup>b</sup> CAS Key Laboratory of Design and Assembly of Functional Nanostructures, Fujian Provincial Key Laboratory of Nanomaterials, Fujian Institute of Research on the Structure of Matter, Chinese Academy of Sciences, 155 Yangqiao Road West, Fuzhou 350002, China

<sup>c</sup> Xiamen Institute of Rare Earth Materials, Xiamen Key Laboratory of Rare Earth Photoelectric Functional Materials, Chinese Academy of Sciences, Xiamen 361021, China

<sup>d</sup> College of Chemistry, Nanchang University, 999 Xuefu Avenue, Nanchang 330031, China.

<sup>e</sup> Department of Materials Science and Engineering, Southern University of Science and Technology, Shenzhen 518055, China.

<sup>f</sup> School of Opto-electronic and Communication Engineering, Xiamen University of Technology, Xiamen 361024, China

† Electronic Supplementary Information (ESI) available: XRD patterns of  $\text{Bi}_2\text{S}_3$  films and absorption spectra of  $(\text{Bi}_{1-x}\text{Sb}_x)_2\text{S}_3$ . See DOI: 10.1039/x0xx00000x

showed a low Seebeck coefficient ( $-21.41 \mu\text{W K}^{-1}$ ) at room temperature (RT).<sup>37</sup> The poor performance indicated that the film fabrication and the carrier concentration need to be appropriately improved.

Up to date, many precursors complexes have been employed for the preparation of solid solution thin films/bulk materials: such as bis(selenobenzoato)dibutyltin(IV) for  $\text{SnS}_{1-x}\text{Se}_x$ ,<sup>38</sup> bis(N,N-diethyl-N'-naphthoylchalcogenoureato)lead(II) for  $\text{PbS}_{1-x}\text{Se}_x$ ,<sup>39</sup> and chalcogeno (thio and seleno) benzoate for  $\text{Sb}_2(\text{S}_{1-x}\text{Se}_x)_3$ .<sup>40</sup> Similarly, significant success has been achieved using the antimony/bismuth complexes of dithiocarbamates,<sup>30,41</sup> dithiophosphates,<sup>42,43</sup> and thiourea,<sup>44,45</sup> as single-source precursors to prepare chalcogenide semiconductors. We chose the metal xanthate precursors to prepare  $\text{Sb}_2\text{S}_3$ <sup>43,46</sup> and  $\text{Bi}_2\text{S}_3$ <sup>37,47</sup> due to the low decomposition temperature of metal xanthate complexes ( $\sim 150^\circ\text{C}$ ), and the advantage of producing oxide-free metal sulfide products compared to the dithiocarbamate complexes via Chugaev elimination<sup>46,48,49</sup> during thermolysis. Concisely, this approach is simple and can produce high-quality metal sulfide with controlled composition. Therefore, we adopted composition engineering by chalcogenide metal-xanthate Precursors (bismuth (III) ethylxanthate) to prepare high-quality  $\text{Bi}_2\text{S}_3$  films on the soda-lime glass by spin-coating and post-annealing steps. Characterization of these as-deposition  $\text{Bi}_2\text{S}_3$  thin films showed a higher Seebeck coefficient of  $-388.33 \mu\text{V K}^{-1}$  than previously reported results for both thin-film<sup>50</sup> and bulk materials<sup>51-53</sup> at RT. The *P.F.* of  $\text{Bi}_2\text{S}_3$  films has a decent value of  $170.10 \mu\text{W m}^{-1} \text{K}^{-2}$ , which approaches nearly 3 times of  $\text{Bi}_2\text{S}_3$  film reported before ( $63.01 \mu\text{W m}^{-1} \text{K}^{-2}$ ).<sup>54</sup> Moreover, the same method was used to synthesize  $(\text{Bi}_{1-x}\text{Sb}_x)_2\text{S}_3$  solid solutions with further improved Seebeck coefficients of  $-516.35 \mu\text{V K}^{-1}$ . This work indicates that composition engineering could be an effective method to enhance the thermoelectric performance of  $\text{Bi}_2\text{S}_3$  films as a promising substitute for telluride-based TE films.

## Experimental

### Chemicals

All the materials and chemicals below were used as received without further treatment. Bismuth nitrate pentahydrate ( $\text{Bi}(\text{NO}_3)_3 \cdot 5\text{H}_2\text{O}$ , 99.99%) was purchased from Aladdin. Potassium ethylxanthate ( $\text{C}_3\text{H}_5\text{KOS}_2$ , 98%) was purchased from Alfa Aesar, Antimony (III) chloride ( $\text{SbCl}_3$ , 99.95%), and chlorobenzene (CB, 99.8%, anhydrous) were purchased from Sigma-Aldrich. Hydrochloric acid (HCl, 36%-38%, AR) and methanol ( $\text{CH}_3\text{OH}$ , AR) were purchased from Xi Long Scientific. Chloroform ( $\text{CHCl}_3$ , AR) was purchased from Sinopharm Chemical Reagent Co., Ltd.

### Instrumentation

The morphology of the samples was inspected using a Field Emission Scanning Electron Microscope (FESEM, Thermo Fisher -Apreo S LoVac). The Energy dispersive spectrometer (EDS) analysis and X-ray dot mapping of  $(\text{Bi}_{1-x}\text{Sb}_x)_2\text{S}_3$  thin films ( $0 \leq x \leq 0.05$ ) was inspected using a Bruker Energy Dispersive X-ray Spectrometer (QUANTAX 200 with XFlash 6/100). Ultraviolet-

visible (UV-vis) absorption spectra were recorded on a Cary 5000 spectrophotometer. The Fourier-transform infrared (FT-IR) spectrums were measured using the Thermo Fisher Nicolet iS 50. The XRD patterns were measured using a Rigaku Miniflex 600 (Cu  $\text{K}\alpha$  radiation,  $\lambda = 1.5418 \text{ \AA}$ ) with an angle range of  $2\theta = 3^\circ$  to  $70^\circ$ . The X-ray photoelectron spectrum was performed using an X-ray photoelectron spectroscopy (XPS) system (Axis Supra, Shimadzu). Element analysis (EA) was measured by Elementar Vari EL Cube. Roman spectrum was obtained by BWS465-785S. The  $^1\text{H}$  NMR spectra were performed on the Bruker AVANCE III 500 MHz spectrometer. Chemical shifts for  $^1\text{H}$  NMR spectra were referenced in the deuterated solvent ( $\text{CHCl}_3$   $\delta = 7.26$  ppm for  $^1\text{H}$ ). Thermogravimetric (TGA) measurements and differential scanning calorimetry (DSC) were carried out on a Mettler Toledo DSC1 at a heat ramp of  $10^\circ\text{C min}^{-1}$  under Argon. The Hall-effect measurements system (HMS5000, Side Semiconductor Technology, Shanghai, China) was measured to obtain electric properties such as carrier concentration, conductivity, mobility of thin films. The thickness of films was determined by Alpha-Step D-600 (KLA, the United States). The electric conductivity was determined by a four-probe method using 4200A-SCS Clarius (Keithley). The Seebeck coefficient was measured by a Keithley 2000 Multimeter (Cleveland, OH, USA). The Seebeck coefficient is defined as  $S = \Delta V / \Delta T$ , where  $\Delta V$  and  $\Delta T$  are the voltage drops across the material and the temperature gradient along with the voltage drop. It was determined by an applied temperature difference of  $\Delta T = 3 \text{ K}$  between the two ends of the samples. In addition, the channel width and the length of the electrode are 1 mm and 7 mm, respectively. All of the measurements were carried out at room temperature.

### Synthesis of bismuth (III) ethylxanthate, $\text{Bi}(\text{S}_2\text{COEt})_3$

The synthesis of  $\text{Bi}(\text{S}_2\text{COEt})_3$  has been well established previously.<sup>55</sup> Typically,  $\text{Bi}(\text{NO}_3)_3 \cdot 5\text{H}_2\text{O}$  (4.8507 g, 10.0mmol) was suspended in an aqueous solution (100 mL) and conc. HCl (36~38% v/v) was added dropwise until a clear solution was obtained. Potassium ethylxanthate (4.8090 g, 30.0 mmol) was dissolved in water (25 mL) and added to the bismuth nitrate solution, and stirred for 30 min. at room temperature. The yellow solid formed was collected by vacuum filtration and recrystallized from a chloroform solution. Elemental analysis (%) found (%): C, 18.86; H, 2.66; S, 33.54. calc (%): C, 18.88; H, 2.64; S, 33.60. IR ( $\text{cm}^{-1}$ ): 1190  $\nu(\text{C}-\text{O})$ ; 1022  $\nu(\text{C}-\text{S})$ .  $^1\text{H}$  NMR ( $\text{CDCl}_3$ ):  $\delta$  4.69 (q,  $J = 7.1 \text{ Hz}$ , 2H,  $\text{CH}_2$ ),  $\delta$  1.49 (t,  $J = 7.1 \text{ Hz}$ , 3H,  $\text{CH}_3$ ).

### Synthesis of antimony (III) ethylxanthate, $\text{Sb}(\text{S}_2\text{COEt})_3$ .

For  $\text{Sb}(\text{S}_2\text{COEt})_3$  preparation, it also had been reported before.<sup>56</sup> Antimony (III) chloride (1.9 g, 8.3 mmol) was dissolved in 25 mL of methanol and added dropwise to a solution of potassium ethylxanthate (4 g, 24.9 mmol) in methanol (100 mL) with constant stirring. The reaction mixture was stirred at room temperature for approximately 30min to ensure the completion of the reaction. The precipitates formed were filtered and dried under vacuum, resulting in a bright yellow solid. The product was recrystallized by dissolving

the precipitates in chloroform and removing the insoluble impurities by filtration. A clear yellow solution was obtained, which on evaporation yielded the pure product. Elemental analysis (%) found (%): C, 22.25; H, 3.12; S, 39.78. calc (%): C, 22.27; H, 3.12; S, 39.63. IR ( $\text{cm}^{-1}$ ): 1221  $\nu(\text{C}-\text{O})$ ; 1020  $\nu(\text{C}-\text{S})$ .  $^1\text{H}$  NMR ( $\text{CDCl}_3$ ):  $\delta$  4.69 (q,  $J = 7.1$  Hz, 2H,  $\text{CH}_2$ ),  $\delta$  1.49 (t,  $J = 7.1$  Hz, 3H,  $\text{CH}_3$ ).

### Preparation of $(\text{Bi}_{1-x}\text{Sb}_x)_2\text{S}_3$ thin films.

$(\text{Bi}_{1-x}\text{Sb}_x)_2\text{S}_3$  thin films with different mole fractions of Sb ( $x = 0, 0.02, 0.03, 0.04, \text{ and } 0.05$ ) were prepared using the composition engineering strategy. Firstly, to prepare the precursor solution, a certain amount of  $\text{Bi}(\text{S}_2\text{COEt})_3$  and  $\text{Sb}(\text{S}_2\text{COEt})_3$  was dissolved in CB and stirred for above 2 h. Then, the precursor solution was filtered and spin-coated onto glass substrate at 900rpm for 9s and 3000rpm for 21s or/and fluorine-doped tin oxide (FTO)-coated glass substrate, which has already been washed (by detergent, deionized water, acetone, and ethanol with the assistance of sonication) and treated by plasma. Finally, it was annealed at 300 °C for 60 s. The spin-coating and post-annealing procedures were repeated four times, and the last time annealed for 10 min to make the film thicker and remove the solvent. This process was performed in an  $\text{N}_2$ -filled glovebox to prevent oxidation.<sup>57</sup>

## Results and discussion

The chalcogenide precursors  $\text{Bi}(\text{S}_2\text{COEt})_3$  and  $\text{Sb}(\text{S}_2\text{COEt})_3$  were prepared according to literature, and the chemical structures were confirmed by  $^1\text{H}$ -NMR.<sup>55</sup> (Fig. S1†) To facilitate the film deposition and post-annealing steps, the thermogravimetric analysis (TGA) and differential scanning calorimetry (DSC) of the chalcogenide precursors  $\text{Bi}(\text{S}_2\text{COEt})_3$  and  $\text{Sb}(\text{S}_2\text{COEt})_3$  were conducted. As shown in Fig. 1A,  $\text{Bi}(\text{S}_2\text{COEt})_3$  exhibited a steep one-step mass loss from 117 °C until 155 °C, with a remaining weight percent of 45.58%, consistent with the calculated (44.95%) composition of inorganic  $\text{Bi}_2\text{S}_3$ . Meanwhile, the DSC analysis shows the melting of bismuth (III) ethylxanthate at  $\sim 117$  °C accompanying the decomposition. The smaller endotherm peak at about 151 °C is probably due to the Chugaev elimination reaction, which leads to the final formation of  $\text{Bi}_2\text{S}_3$ . Similarly, the TGA of  $\text{Sb}(\text{S}_2\text{COEt})_3$  showed decomposition in the temperature range of 100–160 °C, and the minor weight loss of approximately 2% at 243 °C can be ascribed to sulfur removal (Fig. 1B). The final residual mass (35.94%) matches the calculated composition for  $\text{Sb}_2\text{S}_3$  (35.10%).

The X-ray diffraction (XRD) patterns of the as-deposited  $\text{Bi}_2\text{S}_3$  films after annealing at 300 °C are presented in Fig. 1C. The orthorhombic phase of  $\text{Bi}_2\text{S}_3$  is persuasively consistent with the standard JPCDS No.17-0320 PDF card.<sup>47</sup> Some peaks are widened due to the vicinity of the scattering angles of certain planes such as (240) and (420) planes, (020) and (200) lattice planes.<sup>55</sup> Moreover, from the XRD patterns (Fig. S2†), the intensity of diffraction peaks of (130, 301), (210) and (211) gradually increase, indicating that the crystallinity of  $\text{Bi}_2\text{S}_3$  thin film increases with the increase of annealing temperature, and higher temperature led to larger average crystallite size (Fig. 1D). For example, at 220 °C, an average crystallite size of 38.21 nm from the  $\text{Bi}_2\text{S}_3$  film is calculated, which

becomes 2.5 times larger when the annealing temperature reaches 300 °C.

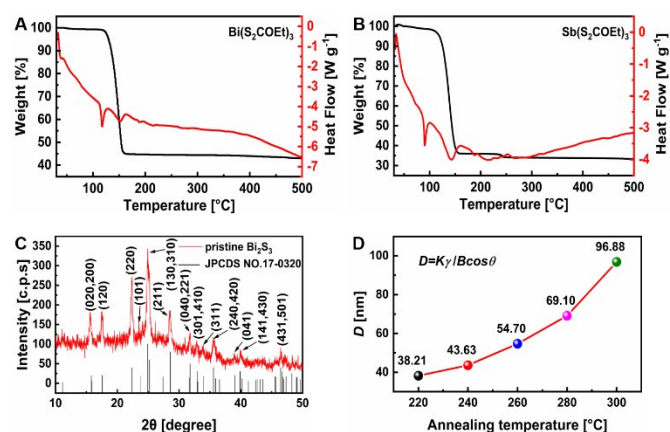
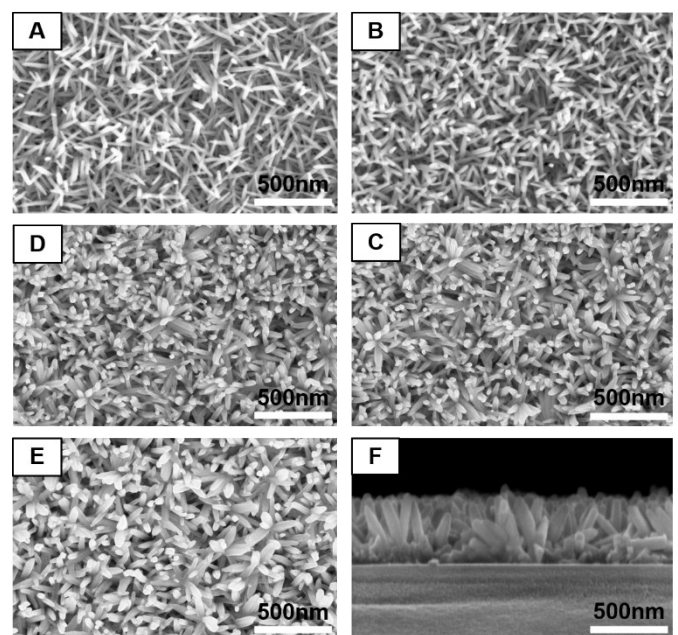


**Fig. 1** (A and B) are TGA and DSC spectra of  $\text{Bi}(\text{S}_2\text{COEt})_3$  and  $\text{Sb}(\text{S}_2\text{COEt})_3$  powders, respectively (conducted under an argon atmosphere). (C) XRD pattern of the as-deposited film (red) after annealing at 300 °C and JPCDS NO.17-0320 (black). (D) Average crystallite sizes ( $D$ ) of  $\text{Bi}_2\text{S}_3$  films annealed at different temperatures.

Fig. 2 shows the surface morphology and cross-section of the  $\text{Bi}_2\text{S}_3$  films after annealing at different temperatures. We speculate that the anisotropic nature of the crystal growth in  $\text{Bi}_2\text{S}_3$  crystals is the reason behind the phenomenon, where the growth along the  $c$  axis is more favored than along the  $a$  and  $b$  axis. According to the Periodic Bond Chain (PBC) theory, the crystal habit is governed by a set of uninterrupted chains of strong bonds formed in the crystal lattice.<sup>58</sup> Therefore, the crystal easily grows along the  $c$  axis because the force of covalent bonds is the strongest among all directions.

**Fig. 2** Topology SEM images of the  $\text{Bi}_2\text{S}_3$  films after annealing at (A) 220 °C, (B)



240 °C, (C) 260 °C, (D) 280 °C (E) 300 °C and (F) 300 °C with higher-resolution on glass.

Moreover, when the temperature increases from 220 °C to 260

°C, the growth rate along the *c* axis is also faster than that of the *a* and *b* axis, resulting in the growth of the rod. As the temperature further increases, the slow growth of crystals along the *a*-axis and *b*-axis could result in the thickening of sharp needles to rods. Thus, as the temperature and crystallite size increase, the morphology changes from an interwoven needle-like network structure to smoother, closely conjoined rods (Fig. 2F), favoring the transfer of carriers.<sup>59</sup> The enlarged average grain size with the increase of annealing temperature is consistent with the XRD analysis. At 300 °C, the Bi<sub>2</sub>S<sub>3</sub> rods with dimensions of approximately 65×500 nm constructs into continuous and compact films. The thickness of Bi<sub>2</sub>S<sub>3</sub> films was controlled by preparing precursor solutions with different concentrations and measured by surface stylus profiler (Table S1†). The conductivity of the films was reported to be strongly influenced by the thickness.<sup>60,61</sup> In our case, the thickness of Bi<sub>2</sub>S<sub>3</sub> film is optimized at 150 nm when the concentration of precursor solution is controlled at 0.2 mol·L<sup>-1</sup>.

As shown in Fig. S3†, the bandgap of Bi<sub>2</sub>S<sub>3</sub> films decreases slightly with the increase of annealing temperature due to the enlarged average crystallite size. After annealing at 300 °C, the bandgap is calculated to be around 1.3 eV (Fig. 3A), consistent with the previous reports.<sup>31</sup> In Fig. 3B, the composition of the Bi<sub>2</sub>S<sub>3</sub> film annealed at 300 °C is investigated by Raman spectroscopy. Three distinctly dominant peaks at 184 cm<sup>-1</sup>, 235 cm<sup>-1</sup>, and 255 cm<sup>-1</sup> can be assigned to the A<sub>g</sub> symmetric bending vibration, A<sub>g</sub> and B<sub>1g</sub> anti-symmetric stretching vibrations, respectively, which agree with the reported data for Bi<sub>2</sub>S<sub>3</sub> prepared by other methods.<sup>62,63</sup>

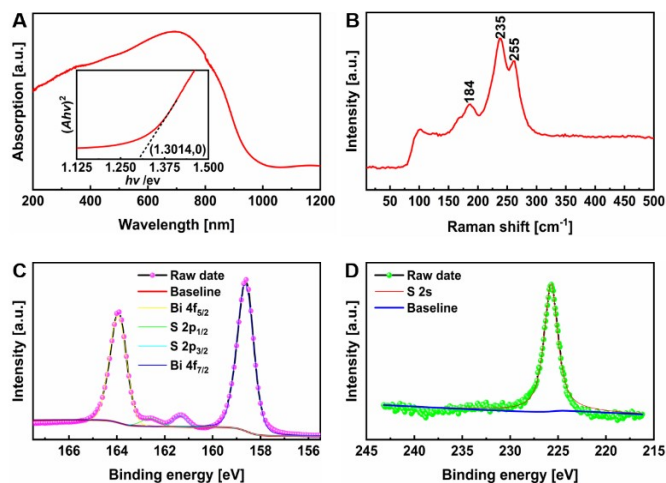


**Fig. 3** (A) Absorbance of the Bi<sub>2</sub>S<sub>3</sub> thin film after annealing at 300 °C, the inset showing the Tauc-plot analysis of Bi<sub>2</sub>S<sub>3</sub> film with the substitution absorption coefficient ( $\alpha$ ) of absorption (A). (B) Raman spectrum (C) XPS core-level spectra of Bi 4f and S 2p. (D) the S 2s spectrum from the Bi<sub>2</sub>S<sub>3</sub> film annealed at 300 °C.

XPS measurements were performed to unveil the valence states and stoichiometric ratio of the as-deposited films. Fig. S4 shows the XPS survey spectrum of a pristine Bi<sub>2</sub>S<sub>3</sub> film annealed at 300 °C. All peaks can be assigned to C, O, Bi, and S elements. The binding energy of the C(1s) transition was used as a reference to calibrate the binding energy of other elements. It is possible that the carbon

signals may come from both the polluting carbon in the environment and the contamination from residual xanthates. According to the thermogravimetry analysis (TGA) of Bi(S<sub>2</sub>COEt)<sub>3</sub> under nitrogen, no organic compound but only carbon could be left when the annealing temperature was 300 °C. In Fig. 3C, the two strong peaks at 158.56 and 163.92 eV can be assigned to Bi 4f<sub>7/2</sub> and Bi 4f<sub>5/2</sub>, respectively, with a typical Bi 4f spin-orbit doublet splitting at 5.36 eV.<sup>64–66</sup> Moreover, the peak at the binding energy of 225.72 eV in Fig. 3D corresponds to the S 2s core level. The calculated elemental ratio (Bi/S: 39.85/60.15) is in good agreement with the stoichiometry of Bi<sub>2</sub>S<sub>3</sub>, which confirms the formation of a stoichiometric Bi<sub>2</sub>S<sub>3</sub>.<sup>67</sup>

Different chalcogenide metal-ligand precursors can be mixed to make solid solutions of Group V metals (Bi<sub>1-x</sub>Sb<sub>x</sub>)<sub>2</sub>S<sub>3</sub> (0 ≤ x ≤ 0.05), via so-called “composition engineering”. The well-defined XRD patterns shown in Fig. S5 indicate the polycrystalline nature and bismuthinite phase of (Bi<sub>1-x</sub>Sb<sub>x</sub>)<sub>2</sub>S<sub>3</sub> films (JCPDS No. 17-0320) after annealing at 300 °C. All samples were confirmed to comprise a single phase with an orthorhombic structure. By the way, as the Sb mole fraction increase, the crystallinity of (Bi<sub>1-x</sub>Sb<sub>x</sub>)<sub>2</sub>S<sub>3</sub> (0 ≤ x ≤ 0.05) films does not change significantly. Moreover, EDX spectrum mapping of the (Bi<sub>1-x</sub>Sb<sub>x</sub>)<sub>2</sub>S<sub>3</sub> samples prepared for all the x values are shown in Fig. S6. It is clearly seen within the range of vision that all the elements (Bi, Sb, and S) were evenly distributed throughout the sample. Afterward, with the increase of ‘x’, the diffraction peak (130) shifts toward higher angles (Fig. 4A) due to the smaller atomic radius of ‘Sb’ (159 pm) than that of ‘Bi’ (170 pm). The substitution of ‘Sb’ in the lattice of Bi<sub>2</sub>S<sub>3</sub> decreases the interplanar spacing and results in a shift of diffraction peaks to higher angles.<sup>56</sup> Furthermore, the change of lattice parameters *a*, *b*, and *c* with the Sb mole fraction can be calculated through the XRD patterns (Fig. S5). The replacement of Bi<sup>3+</sup> by Sb<sup>3+</sup> in the Bi-Sb-S solid solution series increased the *a* and *b* unit cell parameters (Fig. 4B),<sup>68</sup> while the length of the *c*-axis is shortened, which may be due to the decreased M–S bond lengths from Bi<sub>2</sub>S<sub>3</sub> to Sb<sub>2</sub>S<sub>3</sub> and led to the contraction of rods along this direction.<sup>68</sup> (Fig. 4C left, Table S2†).

More information about the solid structure of (Bi<sub>1-x</sub>Sb<sub>x</sub>)<sub>2</sub>S<sub>3</sub> (0 ≤ x ≤ 0.05) films from composition engineering can be extracted from the XRD results (the specific calculation method is described in detail in the supporting information).<sup>27</sup> First, with the increase of the Sb mole fraction, the average crystallite size (*D*) calculated based on Scherrer equation<sup>69,70</sup> decreased (Fig. 4C right), and therefore the number of crystallites per unit area (*N*) increased (Fig. 4D). Finally, the dislocation density ( $\delta$ ) as one of the critical indicators for evaluating the lattice thermal conductivity of the material also goes up when more Bi was gradually replaced by Sb in Bi<sub>2</sub>S<sub>3</sub> lattice, which may result in larger lattice distortion.<sup>71</sup> (Fig. 4E) The specific discussion will be carried out in the thermoelectric properties section.

On the other hand, the optical bandgap of (Bi<sub>1-x</sub>Sb<sub>x</sub>)<sub>2</sub>S<sub>3</sub> solid solutions were calculated based on UV-vis (Fig. S7, S8†). From the Tauc-plots shown in Fig. S8, with the increase of Sb mole fractions from near 0 to 0.05, the calculated direct band gaps increase from 1.46 to 1.59 eV, of which the values lie between intrinsic Bi<sub>2</sub>S<sub>3</sub> and Sb<sub>2</sub>S<sub>3</sub>, i.e., 1.3 and 1.7 eV.<sup>72–74</sup> Fig. S9 reveals the dependence of the

bandgap of the  $(\text{Bi}_{1-x}\text{Sb}_x)_2\text{S}_3$  samples on their compositions, which in turn confirms the formation of a homogeneous solid solution.<sup>56</sup> Meanwhile, a slight deviation from a linear trend is probably due to the stoichiometric variations in the synthesized solid solutions, as has been observed previously.<sup>75</sup>

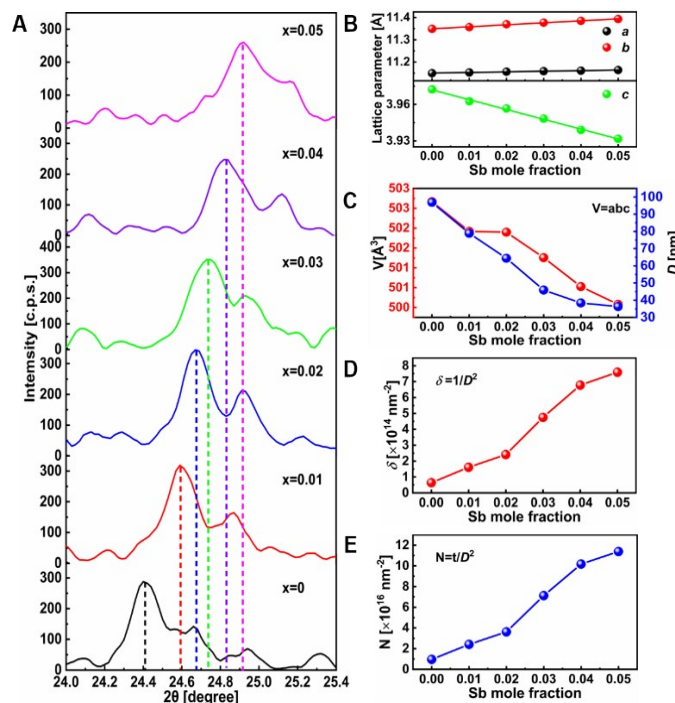


**Fig. 4** XRD analysis of  $(\text{Bi}_{1-x}\text{Sb}_x)_2\text{S}_3$  ( $0 \leq x \leq 0.05$ ) films annealed at 300 °C. (A) Enlarged area of the diffraction peak (130). Change of (B) Lattice parameters. (C) Unit cell volume ( $V$ ) (red line) and average crystallite size (blue line). (D) Number of crystallites per unit area ( $N$ ). (E) Dislocation density ( $\delta$ ).

In order to explore the relationship between Seebeck coefficient and conductivity, the influence of different variables (e.g., annealing temperature, precursor concentration, and Sb content) on the thermoelectric properties of  $(\text{Bi}_{1-x}\text{Sb}_x)_2\text{S}_3$  ( $0 \leq x \leq 0.05$ ) films was investigated by carrying out Hall effect and Seebeck effect measurements. First, Hall effect measurement was applied to determine the carrier concentration ( $n$ ) (Fig. 5A, D, G) and mobility ( $\mu$ ) (Fig. 5B, E, H) of these films, based on which we attained the  $\sigma$  of the films via the equation of  $\sigma = ne\mu$  ( $e$  is electron charge). The Seebeck coefficient was measured by a homemade Seebeck measurement system (See Fig. S10 for the test device diagram in detail) to calculate power factor ( $P.F.$ ) (Fig. 5C, F, I). The four-probe method was also used to measure the conductivity ( $\sigma$ ) for references. (Table S3-5) According to the data of all samples, the volatility of the data is small, indicating high repeatability and good performance stability.

Fig. 5A, B show the  $n$  and  $\mu$  for intrinsic  $\text{Bi}_2\text{S}_3$  films after

annealing at different temperatures when the precursor concentration is set at  $0.25 \text{ mol L}^{-1}$ . With the increase of annealing temperature, the carrier concentration decreases while the carrier mobility increases, which could be explained by reducing the intrinsic defects with higher annealing temperature.<sup>76</sup> Remarkably, the carrier mobility increased from  $1.204$  to  $45.27 \text{ cm V}^{-1} \text{ s}^{-1}$  as the temperature increases from  $220$  to  $300 \text{ }^\circ\text{C}$ , and meanwhile, the carrier concentration decreased an order of magnitude to  $1.977 \times 10^{18} \text{ cm}^{-3}$ , approximately the same level as typical bulk  $\text{Bi}_2\text{S}_3$  material.<sup>77,78</sup> As shown in the XRD measurements, the increased annealing temperature will increase the crystallinity of the film and, hence, decrease the grain boundary density. The gradually reduced intrinsic defects result in the reduction of carrier scattering at grain boundaries and the increase of the mean free path of carriers. Due to a higher increasing rate of the carrier mobility than the decreasing rate of carrier concentration, the electrical conductivity increased to about  $14.32 \text{ S cm}^{-1}$  (Fig. 5C). Meanwhile, since the Seebeck coefficient is inversely proportional to the carrier concentration, as illustrated by

$$S = \frac{8\pi^2 K_B^2}{3eh^2} m^* T \left(\frac{\pi}{3n}\right)^{2/3}$$

Where  $K_B$  is the Boltzmann constant,  $h$  is Planck's constant,  $m^*$  is the effective mass of the charge carrier. The Seebeck coefficient achieved a maximum value of  $344.17 \mu\text{V K}^{-1}$  (Fig. 5C) with the sample annealed at  $300 \text{ }^\circ\text{C}$ , where the  $P.F.$  also reached its peak of  $170.10 \mu\text{W m}^{-1} \text{ K}^{-2}$ .

The dependence of the  $n$  and  $\mu$  of on precursor concentrations is shown in Fig. 5D, E. In this study, all the films were annealed at  $300 \text{ }^\circ\text{C}$ . Fig. 5D shows that the carrier concentration monotonously increases with the increase of precursor concentration due to the added thickness.<sup>79</sup> However, the carrier mobility reaches the maximum at the precursor concentration of  $0.20 \text{ mol L}^{-1}$ , indicating the impact of proper film thickness. (Fig. 5E) As a result, the electrical conductivity also showed the maximum at the concentration of  $0.20 \text{ mol L}^{-1}$ . When the thickness is further increased, the conductivity drops due to higher resistance. (Fig. 5F) As mentioned above, the thickness was about  $150 \text{ nm}$  with a precursor concentration of  $0.20 \text{ mol L}^{-1}$ . At low precursor concentrations ( $0.15$  to  $0.20 \text{ mol L}^{-1}$ ), the carrier concentrations changed slightly since the phonon scattering, which enhances along with the film thickness, played the dominant role. Since the Seebeck coefficient depends mainly on phonon scattering and carrier concentration,<sup>80</sup> the maximal value of Seebeck coefficient appeared at  $0.20 \text{ mol L}^{-1}$  with an improved value of  $-388.33 \mu\text{V K}^{-1}$ . Meanwhile, the  $P.F.$  has also reached the optimal value of  $154.09 \mu\text{W m}^{-1} \text{ K}^{-2}$ . When the precursor concentration is further increased, the carrier concentration becomes the dominant factor, and therefore the Seebeck coefficient drops. Subsequently, the  $P.F.$  decreased gradually, resulting from decreasing in the Seebeck coefficient and electrical conductivity.

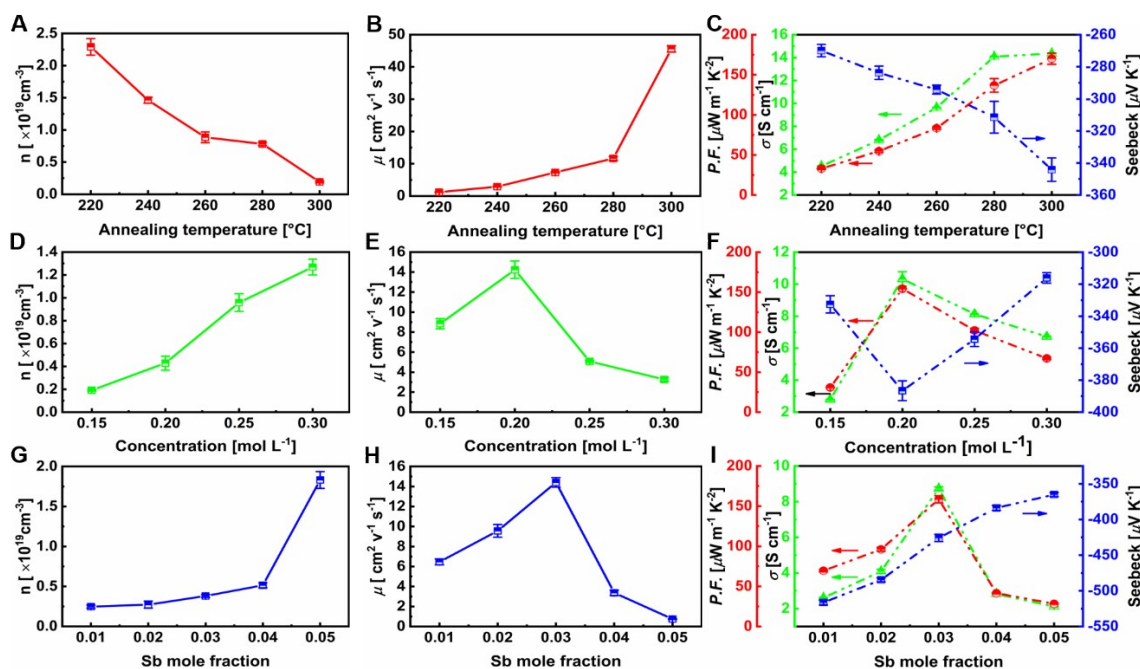


**Fig. 5** Carrier transport and thermoelectric properties of  $(\text{Bi}_{1-x}\text{Sb}_x)_2\text{S}_3$  ( $0 \leq x \leq 0.05$ ) films at R.T. (A and B) Annealing temperature dependences of the  $n$  and  $\mu$ . (C) Annealing temperature dependences of  $\sigma$  (green cross), Seebeck coefficient (blue dot), and  $P.F.$  (red dot). (D and E) Precursor concentration dependences of the  $n$  and  $\mu$  annealing at  $300^\circ\text{C}$ . (F) Precursor concentration dependences on  $\sigma$  (green line), the Seebeck (blue line), and the  $P.F.$  (red line). (G and H) Sb mole fraction dependences of the  $n$  and  $\mu$ . (I) Sb mole fraction dependences of  $\sigma$  (green line), the Seebeck (blue line), and the  $P.F.$  (red line).

It was reported that the mixing of hetero-atoms in an intrinsic TE compound could further improve the Seebeck coefficient.<sup>71,81</sup> There have been reports about incorporating Sb to improve the Seebeck coefficient by manipulating the band structure.<sup>71</sup> Specifically, the incorporation of Sb could tune the effective mass ( $m^*$ ) and resonant states so as to manipulate the band structure of  $\text{Bi}_2\text{S}_3$ . As we know, improving the Seebeck coefficient can be realized by tuning effective mass ( $m^*$ ) and carrier concentration ( $n$ ). After introducing Sb, the valance band is dominated by the Sb-5p and S-3p orbitals,<sup>82</sup> creating a “resonant” state due to distortion on the  $\text{Bi}_2\text{S}_3$  band. When the Fermi level moves close to the resonant state,  $m^*$  becomes significantly increased due to the increased DOS,<sup>83</sup> which has been proven by DFT calculations about thermoelectric properties of the Sb-S System.

In this study, the carrier transport properties of the  $(\text{Bi}_{1-x}\text{Sb}_x)_2\text{S}_3$  ( $0 \leq x \leq 0.05$ ) solid solution films coated with a concentration of  $0.20 \text{ mol L}^{-1}$  and annealed at  $300^\circ\text{C}$  were determined by measuring their  $n$  and  $\mu$ . (Fig. 5G, H). As shown in Fig. 5G, with the increase of the Sb mole fraction, the  $n$  increases indubitably. Nevertheless, the  $\mu$  reached the maximum of  $14.45 \text{ cm}^2 \text{ V}^{-1} \text{ s}^{-1}$  when  $x = 0.03$ , and then decreased with Sb content going higher. It was reported that the  $\mu$  of  $\text{Bi}_2\text{S}_3$  single crystal in the  $c$ -axis direction is higher than that in the  $a$ -axis direction due to the anisotropy of electron-effective mass.<sup>84</sup> Therefore, the gradual shortening of the  $c$ -axis over the range of increasing  $x$  (Fig. 4C) may promote the increase of the  $\mu$ . (*vide supra*) Meanwhile, the decline of the  $\mu$  when the mole fraction of Sb increases could be understood by the dramatically decreased average crystallite size (Fig. 4D).

Upon calculation, the electric transport properties ( $\sigma$ ) of  $(\text{Bi}_{1-x}\text{Sb}_x)_2\text{S}_3$  followed the trend of  $\mu$  and are poorer than those of pure binary  $\text{Bi}_2\text{S}_3$  films. (Fig. 5I, green dots) This could be because the larger bandgap of  $\text{Sb}_2\text{S}_3$  than  $\text{Bi}_2\text{S}_3$  leads to a poorer ability to create sulfur vacancies,<sup>85</sup> which generally act as electron donors to increase the carrier concentration and hence the  $\sigma$ .<sup>77</sup> However, due to the increased dislocation density with more Sb substitution (Fig. 4F), the phonon scattering of those ternary films was enhanced and led to lower lattice thermal conductivity, which is theoretically beneficial for improving the Seebeck coefficient.<sup>71</sup> Besides, the  $(\text{Bi}_{1-x}\text{Sb}_x)_2\text{S}_3$  films with small crystallite sizes and more crystallites possess large amounts of crystallite boundary barriers, which may play a role of energy filter to screen out low energy carriers, thus leading to an increase of Seebeck coefficient.<sup>23,71</sup> As expected, the  $(\text{Bi}_{1-x}\text{Sb}_x)_2\text{S}_3$  thermoelectric thin films showed a further increased Seebeck coefficient of  $-516.35 \mu\text{V K}^{-1}$ . The introduction of Sb by chalcogenide metal-ligands engineering effectively improved the Seebeck coefficient of intrinsic  $\text{Bi}_2\text{S}_3$  film. Nevertheless, the  $P.F.$  declined slightly due to the decrease in electric conductivity. Additionally, for comparison, the thermoelectric properties of other previously reported TEFs or bulk at room temperature are listed in Table S6. It is found that the thermoelectric performance of thin films fabricated by our method in the present work is higher than most other works except Ref. 9 due to different fabrication and measuring conditions. Consequently, the composition engineering approach could pave the way for developing other high-performance low-temperature chalcogenides-based thermoelectric thin films.

## Conclusions

In summary, a series of high-quality  $(\text{Bi}_{1-x}\text{Sb}_x)_2\text{S}_3$  ( $0 \leq x \leq 0.05$ ) thin films with high room-temperature thermoelectric performance via a unique composition engineering protocol has been prepared. With higher annealing temperature and due to the much-enhanced  $\mu$  and  $\sigma$  thereof, the power factor arrives at the optimum point of  $170.10 \mu\text{W m}^{-1} \text{K}^{-2}$  at RT, which is a vital breakthrough for  $\text{Bi}_2\text{S}_3$  thermoelectric thin film. Notably, the achieved high Seebeck coefficient of  $-388.33 \mu\text{V K}^{-1}$  exceeded that of the reported  $\text{Bi}_2\text{S}_3$  bulk material ( $-352 \mu\text{V K}^{-1}$ ). Subsequently, the effect of Sb-doping was investigated to promote the thermoelectric properties further. As a result, it was motivated to see that the  $(\text{Bi}_{0.97}\text{Sb}_{0.03})_2\text{S}_3$  film acquired the even higher Seebeck coefficient of  $-516.35 \mu\text{V K}^{-1}$ . With this work, we realized  $\text{Bi}_2\text{S}_3$  derivatives as the high-performance room-temperature thermoelectric material through the chalcogenide metal-ligands composition engineering. We expect the method to be extended to other thin-film thermoelectric materials and broaden the choice of room-temperature TEFs for wearing microelectronic devices.

## Author Contributions

**Zhenyu Hu:** Conceptualization, Validation, Formal analysis, Investigation, Writing-original draft, Writing-review & editing. **Longhui Deng:** Methodology. **Tingjun Wu:** Software. **Jing Wang:** Visualization. **Feiyan Wu:** Writing-Review & Editing. **Lie Chen:** Project administration. **QiKai Li:** Visualization. **Weishu Liu:** Project administration. **Shuiyang Lien:** Data Curation. **Peng Gao:** Resources, Supervision, Project administration, Funding acquisition, Writing-Review & Editing.

## Conflicts of interest

There are no conflicts of interest to declare.

## Acknowledgments

P.G. acknowledges the financial support from the “Hundred Talents Program” of the Haixi Institute Chinese Academy of Sciences and Fujian Province and the “Global Talent Recruitment Program” of the Government of China.

## Notes and references

- 1 T. Zhu, Y. Liu, C. Fu, J. P. Heremans, J. G. Snyder and X. Zhao, *Adv. Mater.*, 2017, **29**, 1605884.
- 2 C. Gayner and K. K. Kar, *Prog. Mater. Sci.*, 2016, **83**, 330–382.
- 3 M. Liu, M. B. Johnston and H. J. Snaith, *Nature*, 2013, **501**, 395–398.
- 4 J. Burschka, N. Pellet, S. J. Moon, R. Humphry-Baker, P. Gao, M. K. Nazeeeruddin and M. Grätzel, *Nature*, 2013, **499**, 316–319.
- 5 Z. Dong, J. Tan, E. Muljadi, R. M. Nelms, A. St-Hilaire, M. Pevarnik and M. D. Jacobson, *IEEE Trans. Sustain. Energy*, 2020, **11**, 2870–2878.
- 6 O. Ellabban, H. Abu-Rub and F. Blaabjerg, *Renew. Sustain. Energy Rev.*, 2014, **39**, 748–764.
- 7 S. J. Zinkle and G. S. Was, *Acta Mater.*, 2013, **61**, 735–758.
- 8 G. H. Marcus, *Prog. Nucl. Energy*, 2000, **37**, 5–10.
- 9 D. Beretta, N. Neophytou, J. M. Hodges, M. G. Kanatzidis, D. Narducci, M. Martin-Gonzalez, M. Beekman, B. Balke, G. Cerretti, W. Tremel, A. Zevalkink, A. I. Hofmann, C. Müller, B. Dörling, M. Campoy-Quiles and M. Caironi, *Mater. Sci. Eng. R Reports*, 2019, **138**, 210–255.
- 10 C. Liu, F. Li, M. Lai-Peng and H. M. Cheng, *Adv. Mater.*, 2010, **22**, 28–62.
- 11 T. J. Seebeck, *Mitteilungen der Phys. Gesellschaft Zürich*, 1916, **18**, 47–62.
- 12 Z. Bu, X. Zhang, B. Shan, J. Tang, H. Liu, Z. Chen, S. Lin, W. Li and Y. Pei, *Sci. Adv.*, 2021, **7**, eabf2738.
- 13 P. Ying, R. He, J. Mao, Q. Zhang, H. Reith, J. Sui, Z. Ren, K. Nielsch and G. Schierning, *Nat. Commun.*, 2021, **12**, 1121.
- 14 S. Roychowdhury, T. Ghosh, R. Arora, M. Samanta, L. Xie, N. K. Singh, A. Soni, J. He, U. V. Waghmare and K. Biswas, *Science (80- )*, 2021, **371**, 722–727.
- 15 A. I. Hochbaum, R. Chen, R. D. Delgado, W. Liang, E. C. Garnett, M. Najarian, A. Majumdar and P. Yang, *Nature*, 2008, **451**, 163–167.
- 16 G. J. Snyder and E. S. Toberer, *Nat. Mater.*, 2008, **7**, 105–114.
- 17 J. Shuai, J. Mao, S. Song, Q. Zhang, G. Chen and Z. Ren, *Mater. Today Phys.*, 2017, **1**, 74–95.
- 18 C. J. Vineis, A. Shakouri, A. Majumdar and M. G. Kanatzidis, *Adv. Mater.*, 2010, **22**, 3970–3980.
- 19 Q. H. Zhang, X. Y. Huang, S. Q. Bai, X. Shi, C. Uher and L. D. Chen, *Adv. Eng. Mater.*, 2016, **18**, 194–213.
- 20 L. Hicks and M. S. Dresselhaus, *Phys. Rev. B*, 1993, **47**, 8–11.
- 21 Y. F. Hu, E. Sutter, W. D. Si and Q. Li, *Appl. Phys. Lett.*, 2005, **87**, 171912.
- 22 T. Wu and P. Gao, *Materials (Basel)*, 2018, **11**, 999.
- 23 S.-C. Liufu, L.-D. Chen, Q. Yao and C.-F. Wang, *Appl. Phys. Lett.*, 2007, **90**, 112106.
- 24 R. Venkatasubramanian, E. Siivola, T. Colpitts and B. O’Quinn, *Nature*, 2001, **413**, 597–602.
- 25 S. D. Lakade, *UGC CARE J.*, 2020, **31**, 1285–1292.
- 26 F. Ding, Q. Wang, S. Zhou, G. Zhao, Y. Ye and R. Ghomashchi, *R. Soc. Open Sci.*, 2020, **7**, 200479.
- 27 R. S. Lokhande, S. R. Thakur and P. A. Chate, *Optik (Stuttg.)*, 2020, **219**, 165230.
- 28 H. Moreno-García, S. Messina, M. Calixto-Rodriguez and H. Martínez, *Appl. Surf. Sci.*, 2014, **311**, 729–733.
- 29 O. Dachraoui, J. M. Merino, A. Mami, M. León, R. Caballero and H. Maghraoui-Meherzi, *Appl. Phys. A*, 2018, **124**, 166.
- 30 O. C. Monteiro, T. Trindade, J. H. Park and P. O’Brien, *Chem. Vap. Depos.*, 2000, **6**, 230–232.
- 31 J. Waters, D. Crouch, J. Raftery and P. O’Brien, *Chem. Mater.*, 2004, **16**, 3289–3298.
- 32 M. Medles, N. Benramdane, A. Bouzidi, A. Nakrela, H. Tabet-Derraz, Z. Kebbab, C. Mathieu, B. Khelifa and R. Desfeux, *Thin Solid Films*, 2006, **497**, 58–64.
- 33 Z. Kebbab, N. Benramdane, M. Medles, A. Bouzidi and H. Tabet-Derraz, *Sol. Energy Mater. Sol. Cells*, 2002, **71**, 449–457.
- 34 P. A. Chate and S. D. Lakde, *J. Mater. Sci. Mater. Electron.*, 2015, **26**, 5847–5851.
- 35 S. S. Raut, J. A. Dhobale and B. R. Sankapal, *Phys. E Low-dimensional Syst. Nanostructures*, 2017, **87**, 209–212.
- 36 Y. Wang, J. Chen, L. Jiang, F. Liu, Y. Lai and J. Li, *Mater. Lett.*, 2017, **209**, 479–482.

- 37 J. Recatala-Gomez, H. K. Ng, P. Kumar, A. Suwardi, M. Zheng, M. Asbahi, S. Tripathy, I. Nandhakumar, M. S. M. Saifullah and K. Hippalgaonkar, *ACS Appl. Mater. Interfaces*, 2020, **12**, 33647–33655.
- 38 M. D. Khan, M. Aamir, G. Murtaza, M. A. Malik and N. Revaprasadu, *Dalt. Trans.*, 2018, **47**, 10025–10034.
- 39 S. A. Saah, M. D. Khan, P. D. McNaughten, J. A. M. Awudza, N. Revaprasadu and P. O'Brien, *New J. Chem.*, 2018, **42**, 16602–16607.
- 40 M. D. Khan, S. U. Awan, C. Zequine, C. Zhang, R. K. Gupta and N. Revaprasadu, *ACS Appl. Energy Mater.*, 2020, **3**, 1448–1460.
- 41 J. Rodriguez-Castro, M. F. Mahon and K. C. Molloy, *Chem. Vap. Depos.*, 2006, **12**, 601–607.
- 42 W. Lou, M. Chen, X. Wang and W. Liu, *Chem. Mater.*, 2007, **19**, 872–878.
- 43 J. R. Castro, K. C. Molloy, Y. Liu, C. S. Lai, Z. Dong, T. J. White and E. R. T. Tiekink, *J. Mater. Chem.*, 2008, **18**, 5399–5405.
- 44 C. L. McCarthy, D. H. Webber, E. C. Schueller and R. L. Brutchey, *Angew. Chemie - Int. Ed.*, 2015, **54**, 8378–8381.
- 45 Tarachand, V. Sharma, R. Bhatt, V. Ganesan and G. S. Okram, *Nano Res.*, 2016, **9**, 3291–3304.
- 46 T. Alqahtani, R. J. Cernik, P. O'Brien and D. J. Lewis, *J. Mater. Chem. C*, 2019, **7**, 5112–5121.
- 47 R. Nishikubo and A. Saeki, *J. Phys. Chem. Lett.*, 2018, **9**, 5392–5399.
- 48 Y. T. Alharbi, F. Alam, A. Salhi, M. Missous and D. J. Lewis, *Sci. Rep.*, 2021, **11**, 3053.
- 49 M. D. Khan, M. Aamir, M. Sohail, S. Bhoyate, M. Hyatt, R. K. Gupta, M. Sher and N. Revaprasadu, *Dalt. Trans.*, 2019, **48**, 3714–3722.
- 50 N. P. Klochko, V. R. Kopach, I. I. Tyukhov, G. S. Khrypunov, V. E. Korsun, V. O. Nikitin, V. M. Lyubov, M. V. Kirichenko, O. N. Otchenashko, D. O. Zhadan, M. O. Maslak and A. L. Khrypunova, *Sol. Energy*, 2017, **157**, 657–666.
- 51 Z. H. Ge, B. P. Zhang, Z. X. Yu and J. F. Li, *J. Mater. Res.*, 2011, **26**, 2711–2718.
- 52 Tarachand, G. S. Okram, B. K. De, S. Dam, S. Hussain, V. Sathe, U. Deshpande, A. Lakhani and Y. K. Kuo, *ACS Appl. Mater. Interfaces*, 2020, **12**, 37248–37257.
- 53 K. Biswas, L.-D. Zhao and M. G. Kanatzidis, *Adv. Energy Mater.*, 2012, **2**, 634–638.
- 54 Q. Yang, C. Hu, S. Wang, Y. Xi and K. Zhang, *J. Phys. Chem. C*, 2013, **117**, 5515–5520.
- 55 A. J. Maclachlan, F. T. F. O'Mahony, A. L. Sudlow, M. S. Hill, K. C. Molloy, J. Nelson and S. A. Haque, *ChemPhysChem*, 2014, **15**, 1019–1023.
- 56 T. Alqahtani, M. D. Khan, D. J. Kelly, S. J. Haigh, D. J. Lewis and P. O'Brien, *J. Mater. Chem. C*, 2018, **6**, 12652–12659.
- 57 R. Nishikubo, H. Kanda, I. García-Benito, A. Molina-Ontoria, G. Pozzi, A. M. Asiri, M. K. Nazeeruddin and A. Saeki, *Chem. Mater.*, 2020, **32**, 6416–6424.
- 58 J. R. Rumble, D. M. Bickham and C. J. Powell, *Surf. Interface Anal.*, 1992, **19**, 241–246.
- 59 S. C. Liufu, L. D. Chen, Q. Wang and Q. Yao, *Cryst. Growth Des.*, 2007, **7**, 639–643.
- 60 R. Tang, X. Wang, W. Lian, J. Huang, Q. Wei, M. Huang, Y. Yin, C. Jiang, S. Yang, G. Xing, S. Chen, C. Zhu, X. Hao, M. A. Green and T. Chen, *Nat. Energy*, 2020, **5**, 587–595.
- 61 C. Wu, C. Jiang, X. Wang, H. Ding, H. Ju, L. Zhang, T. Chen and C. Zhu, *ACS Appl. Mater. Interfaces*, 2019, **11**, 3207–3213.
- 62 K. A. Messalea, A. Zavabeti, M. Mohiuddin, N. Syed, A. Jannat, P. Atkin, T. Ahmed, S. Walia, C. F. McConville, K. Kalantar-Zadeh, N. Mahmood, K. Khoshmanesh and T. Daeneke, *Adv. Mater. Interfaces*, 2020, **7**, 2001131.
- 63 V. Kaltenhauser, T. Rath, W. Haas, A. Torvisco, S. K. Müller, B. Friedel, B. Kunert, R. Saf, F. Hofer and G. Trimmel, *J. Mater. Chem. C*, 2013, **1**, 7825–7832.
- 64 W. E. Morgan, W. J. Stec and J. R. Van Wazer, *Inorg. Chem.*, 1973, **12**, 953–955.
- 65 M. W. Chu, M. Ganne, M. T. Caldes and L. Brohan, *J. Appl. Phys.*, 2002, **91**, 3178–3187.
- 66 Y. Zhao, Y. Xie, J. S. Jie, C. Y. Wu and S. Yan, *J. Mater. Chem.*, 2009, **19**, 3378–3383.
- 67 N. Huo, A. Figueroba, Y. Yang, S. Christodoulou, A. Stavrinadis, C. Magén and G. Konstantatos, *Adv. Opt. Mater.*, 2019, **7**, 1900258.
- 68 D. Poleti, L. Karanović, T. Balić-Žunić and I. Gržetić, *Neues Jahrb. für Mineral. Abhandlungen*, 2012, **189**, 177–187.
- 69 M. Dhanam, R. R. Prabhu and P. K. Manoj, *Mater. Chem. Phys.*, 2008, **107**, 289–296.
- 70 P. A. Chate and V. D. Bhabad, *Int. J. Mod. Trends Sci. Technol.*, 2016, **2**, 6–11.
- 71 L. Yang, Z. Chen, M. S. Dargusch and J. Zou, *Adv. Energy Mater.*, 2018, **8**, 1701797.
- 72 J. Han, S. Wang, J. Yang, S. Guo, Q. Cao, H. Tang, X. Pu, B. Gao and X. Li, *ACS Appl. Mater. Interfaces*, 2020, **12**, 4970–4979.
- 73 V. K. Perla, S. K. Ghosh and K. Mallick, *J. Mater. Chem. C*, 2021, **9**, 6904–6910.
- 74 Q. Han, J. Chen, X. Yang, D. Lu and X. Wang, *J. Phys. Chem. C*, 2007, **111**, 14072–14077.
- 75 V. A. Patil, A. R. Patil, J.-W. Choi, D. S. Paik and S.-J. Yoon, *Surf. Eng.*, 2007, **23**, 28–31.
- 76 B. Fang, Z. Zeng, X. Yan and Z. Hu, *J. Mater. Sci.*, 2013, **48**, 4408–4415.
- 77 B. Chen, C. Uher, L. Iordanidis and M. G. Kanatzidis, *Chem. Mater.*, 1997, **9**, 1655–1658.
- 78 K. Biswas, L. D. Zhao and M. G. Kanatzidis, *Adv. Energy Mater.*, 2012, **2**, 634–638.
- 79 S.-C. Liufu, L.-D. Chen, Q. Yao and C.-F. Wang, *J. Phys. Chem. B*, 2006, **110**, 24054–24061.
- 80 Z. Zhang, Y. Wang, Y. Deng and Y. Xu, *Solid State Commun.*, 2011, **151**, 1520–1523.
- 81 D. Li, Y. Gong, Y. Chen, J. Lin, Q. Khan, Y. Zhang, Y. Li, H. Zhang and H. Xie, *Nano-Micro Lett.*, 2020, **12**, 36.
- 82 T. Ben Nasr, H. Maghraoui-Meherzi and N. Kamoun-Turki, *J. Alloys Compd.*, 2016, **663**, 123–127.
- 83 J. P. Heremans, B. Wiendlocha and A. M. Chamoire, *Energy Environ. Sci.*, 2012, **5**, 5510–5530.
- 84 A. Cantarero, J. Martinez-Pastor, A. Segura and A. Chevy, *Phys. Rev. B*, 1987, **35**, 9586–9590.
- 85 Y. Kawamoto and H. Iwasaki, *J. Electron. Mater.*, 2014, **43**, 1475–1479.